Optics Letters

Slow light waveguides in topological valley photonic crystals

Hironobu Yoshimi,[1,2,*] Takuto Yamaguchi,[1,2] Yasutomo Ota,[3] Yasuhiko Arakawa,[3] and Satoshi Iwamoto[1,2,3]

[1]Research Center for Advanced Science and Technology, The University of Tokyo, 4-6-1 Komaba, Meguro-ku, Tokyo 153-8505, Japan
[2]Institute of Industrial Science, The University of Tokyo, 4-6-1 Komaba, Meguro-ku, Tokyo 153-8505, Japan
[3]Institute for Nano Quantum Information Electronics, The University of Tokyo, 4-6-1 Komaba, Meguro-ku, Tokyo 153-8505, Japan
*Corresponding author: hyoshimi@iis.u-tokyo.ac.jp

Received 6 March 2020; revised 1 April 2020; accepted 4 April 2020; posted 6 April 2020 (Doc. ID 391764); published 30 April 2020

Valley photonic crystals (VPhCs) are an attractive platform for the implementation of topologically protected optical waveguides in photonic integrated circuits (PICs). The realization of slow light modes in the topological waveguides may lead to further miniaturization and functionalization of the PICs. In this Letter, we report an approach to realize topological slow light waveguides in semiconductor-slab-based VPhCs. We show that a bearded interface of two topologically distinct VPhCs can support topological kink modes with large group indices over 100 within the topological bandgap. We numerically demonstrate robust light propagation in the topological slow light waveguide with large group indices of ∼60, even under the presence of sharp bends. Our work opens a novel route to implement topological slow light waveguides in a way compatible with current PIC technology.

https://doi.org/10.1364/OL.391764

Topological photonic crystals (PhCs) attract enormous attention because of their potential to realize advanced waveguides, which are supported at the perimeters of the bulk PhCs and are immune to certain disorders [1–3]. So far, chiral and helical edge states, respectively, in quantum-Hall-like and quantum-spin-Hall-like photonic systems have been demonstrated to function as robust optical waveguides [4–12]. They are predominantly realized with gyromagnetic materials, bulky photonic systems, and/or leaky modes, and therefore waiting for a technological leap to be compatible with current photonic integrated circuit (PIC) technology.

Recently, kink states in valley photonic crystals (VPhCs) have been proposed and demonstrated to function as topologically protected optical waveguides [13–31]. They are formed at the interfaces of two topologically different VPhCs with bandgaps induced by breaking spatial inversion symmetry. VPhCs can be realized only using dielectrics and can be designed to support topological kink modes below the light line that operates in the telecommunication wavelengths. Such topological VPhC waveguides are known to enable dense integration with footprints comparable to conventional PhCs and enable robust light transport even through sharp waveguide corners, as far as inter-valley scattering is suppressed [14]. These properties are highly desirable for realizing densely integrated low-loss PICs.

Further downscaling and functionalization of PICs could be expected in the case of introducing slow light modes in topological waveguides. However, topological interface modes by nature behave as fast light modes by crossing the bandgap with linear dispersions. This inherent behavior is notably known for edge states of topological insulators and poses a challenge in realizing high-group-index topological waveguides. A few novel ideas have been proposed in previous reports for realizing slow light topological waveguides [32–36]. However, they are based on complex structures, such as gyromagnetic PhCs or bianisotropic metamaterials, which are challenging to implement in PICs.

In this Letter we report a novel method for realizing topological slow light waveguides in semiconductor-slab-based VPhCs. We found that a bearded interface [37] in the VPhCs can support a valley kink state with high group indices (n_gs) within the topological bandgap. With numerical simulations, we demonstrate robust light transmission via the slow light mode, even under the presence of sharp waveguide bends. We identify the origin of the waveguide modes in the bearded interface by comparing it with a zigzag interface, which has been commonly investigated for VPhC waveguides to date. The proposed VPhC waveguide is highly compatible with the PIC technology and could be applied to a wide range of devices, including compact optical delay lines and functional light channels with enhanced light–matter interactions. We expect that introducing topological protection could mitigate some notorious issues in slow light waveguides, such as increased back-reflection and large bending loss [38,39].

Figure 1(a) shows a schematic of the VPhC waveguide investigated here. The structure is constituted of two topologically different VPhCs, type A (colored in blue) and type B (colored in red), interfaced with each other. The unit cells of the two VPhCs are shown in Fig. 1(b). Equilateral triangular airholes with side lengths L_L and L_S are patterned in a honeycomb lattice with a common lattice constant a. When $L_L = L_S$, the system possesses C_{6v} symmetry and supports a symmetry-protected gapless band structure between the first and second lowest energy bands [24]. When $L_L \neq L_S$, the system breaks the spatial inversion symmetry, and a topological bandgap opens between

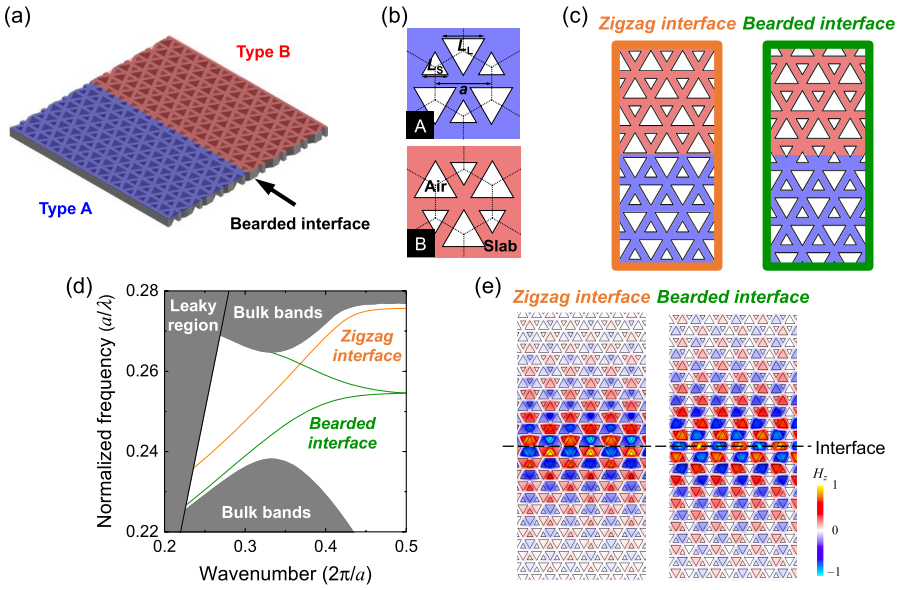

Fig. 1. (a) Schematic of the VPhC waveguide. (b) Schematic of the unit cells of the VPhCs. (c) Schematic of the zigzag and bearded interfaces formed between two topologically distinct VPhCs. (d) Dispersion curves for the edge states formed at the zigzag (orange curve) and bearded (green) interfaces with $L_L = 1.3a/\sqrt{3}$ and $L_S = 0.7a/\sqrt{3}$. The edge states at the bearded interface support slow light regime near the BZ edge. (e) Mode distributions for the edge states formed at the zigzag and bearded interfaces, calculated at a wavenumber of $0.33(2\pi/a)$.

the two bands. The two gapped bands are topologically distinct and can be characterized by valley Chern numbers. In addition, the topological nature within one particular band differs between K and K' valleys and between type A and type B VPhCs. Corresponding valley Chern numbers for the first band around K valley are $-1/2$ and $+1/2$, respectively, for type A and type B VPhCs [16,17]. The distinct topological properties are a prerequisite for generating topological edge states at the interface of the two VPhCs.

Figure 1(c) shows two types of interfaces formed between the two VPhCs. The left panel shows a zigzag interface that faces larger airholes at the boundary. This type of interface, together with that facing smaller holes, has been predominantly investigated for VPhC waveguides so far. In the current work, we employ a different type of interface, called a bearded interface [37], shown in the right panel of Fig. 1(c). We focus on a bearded interface jointing smaller airholes. Figure 1(d) shows computed dispersion curves for the edge states at the zigzag (orange curve) and bearded (green) interfaces with $L_L = 1.3a/\sqrt{3}$ and $L_S = 0.7a/\sqrt{3}$. The simulations were performed for transverse electric field mode by the two-dimensional plane wave expansion method. The refractive index of silicon was set to 3.4. In-gap edge states can be confirmed for both interfaces. The zigzag interface supports a single mode that behaves as a fast light mode within the topological bandgap. In contrast, the bearded interface does two confined modes: one corresponds to a topological edge state, and the other does a trivial state, as discussed later. They exhibit heavily bent dispersions, resulting in the formation of slow light modes within the gap. The two modes are degenerate at the Brillouin zone (BZ) edge, which is forced by glide plane symmetry of the interface [40]. Similar bent and degenerate dispersion curves have also been reported in glided PhC waveguides based on line defects [41,42]. It is noteworthy that similar dispersion curves can also be found for the other bearded interface facing larger airholes [17]. However, they do not seem to exhibit slow light region within the bulk bandgap.

Figure 1(e) shows mode distributions for the kink modes calculated at a wavenumber of $0.33(2\pi/a)$. For the bearded interface, the distribution of the lower energy band was plotted. For both cases, light localization near the interface is as expected. The lateral distributions of the two modes differ in the positions of nodes and anti-nodes with respect to the interfaces. The zigzag interface mode exhibits nodes at the interface, while the bearded interface mode does anti-nodes. Meanwhile, the two field distributions are overall similar to each other after shifting the origin of the center of one of the graph plots perpendicular to the propagation direction. The reason for this coincidence will be addressed later.

Next, we investigate the origins of the guided modes at the bearded interface by exploiting the fact that the zigzag and bearded interfaces can be adiabatically transformed to each other by changing airhole sizes adjacent to the interface. Figure 2(a) shows a gradual transformation of the interface by modifying the sizes of airholes colored in red (side length L_R). It is clearly seen that the zigzag interface ($L_R = 1.3a/\sqrt{3}$) is transformed to the bearded interface ($L_R = 0.7a/\sqrt{3}$) accompanied by a shift in the position of interface. Corresponding dispersion curves for the modified interfaces are plotted in Fig. 2(b). The curve for the zigzag interface (shown in orange) is the same as the one presented in Fig. 1(d) and is of the topological edge state, as has been confirmed in the previous study [16]. Decreasing L_R results in locally increasing refractive index around the interface, leading to the lowering of frequency of the topological kink state, as well as the emergence of a trivial mode near the high-frequency bulk band edge, as seen in the purple ($L_R = 1.1a/\sqrt{3}$) and light blue ($L_R = 0.9a/\sqrt{3}$) curves in Fig. 2(b). For $L_R = 0.7a/\sqrt{3}$ (green curve), the two dispersion

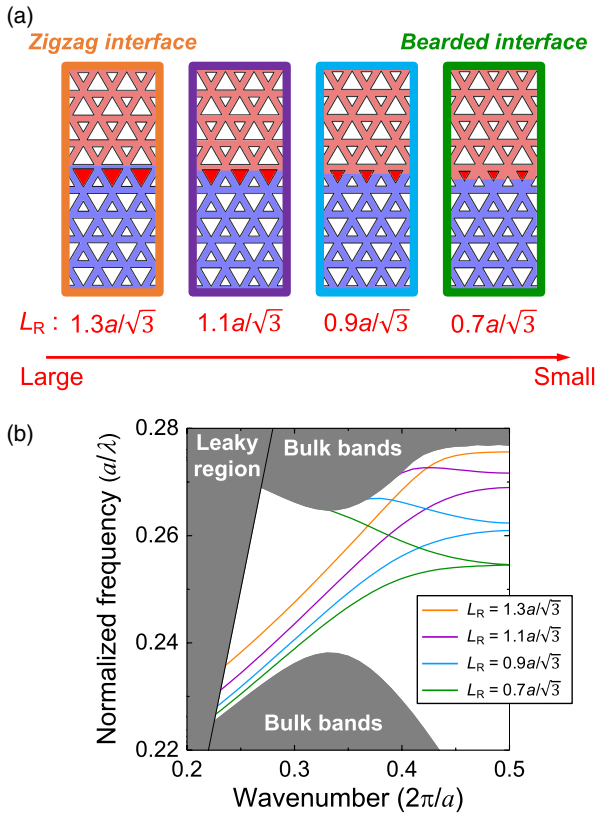

Fig. 2. (a) Interface structures for various sizes of the red triangular air holes. Each panel corresponds to the following conditions: $L_R = 1.3a/\sqrt{3}$, $1.1a/\sqrt{3}$, $0.9a/\sqrt{3}$, and $0.7a/\sqrt{3}$. (b) Dispersion curves of the edge states supported at the interfaces in Fig. 2(a).

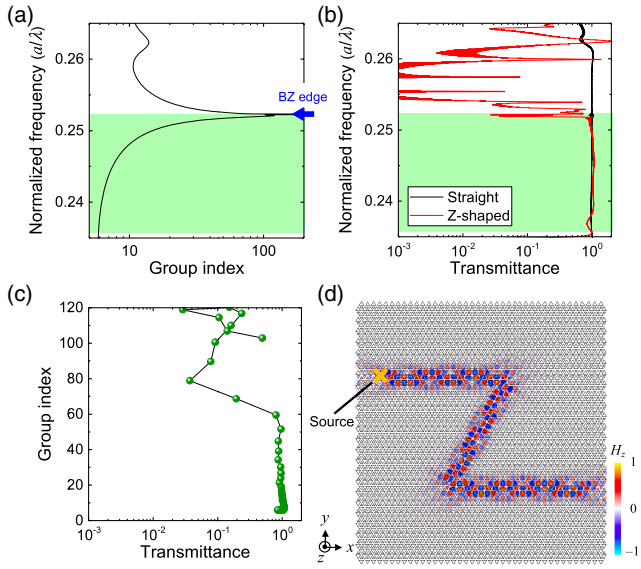

Fig. 3. (a) Calculated group indices for the edge states at the bearded interfaces with $L_L = 1.3a/\sqrt{3}$ and $L_S = 0.7a/\sqrt{3}$ as a function of normalized frequency by the two-dimensional plane wave expansion method. (b) Calculated transmission spectra for straight (black curve) and Z-shaped (red) interfaces. The green region in (a) and (b) indicates the single-mode operation band of the topological edge modes. (c) Transmittance of the Z-shaped interface for the single mode operation band of the topological edge mode as a function of group indices. (d) Magnetic (H_z) field distribution of light propagating through a Z-shaped interface. The normalized frequency of the propagating light is $f = 0.2514$ (a/λ), which corresponds to the group velocity $n_g \sim 30$.

curves merge at the BZ edge since the system forms the bearded interface and, hence, recovers glide plane symmetry. Given that each optical mode is adiabatically modified during changes in L_R, it is reasonable to assign the lower energy modes among the two modes for the bearded interface as the topological mode, similar to that in the zigzag case. Then, the resemblance of the two mode distributions in Fig. 1(e) can be naturally understood, since the topological modes in the zigzag and bearded cases differ only by the influence of the local index perturbation with varying L_R. According to the above discussion, the higher frequency mode at the bearded interface can be assigned as a trivial mode.

The emergence of the trivial mode that lowers its frequency with decreasing L_R, together with its forced degeneracy with the topological mode at the BZ edge, causes the strong bending of the two dispersion curves. This results in the appearance of the slow light modes within the bulk bandgap. The presence of the full two-dimensional bandgap and the topological origin of the lower-frequency mode suggests the possibility of robust light transport as a slow light waveguide. We note that, when the asymmetry between L_L and L_S is small, the lower frequency edge mode crosses the bulk bandgap without significant bending. This observation additionally supports the conclusion that the lower (higher) frequency edge mode originates from a topological kink (trivial) state.

We calculated n_gs for the confined modes of the bearded interface with $L_L = 1.3a/\sqrt{3}$ and $L_S = 0.7a/\sqrt{3}$ as a function of normalized frequency, and we plotted them in Fig. 3(a). The bandwidth of single-mode operation of the topological edge state ranges from $a/\lambda = 0.2358 \sim 0.2523$, and it is indicated by the green shading. In the plot, a sharp increase in n_g is confirmed near the BZ edge, and n_g reaches the highest value of 120 at a normalized frequency of $a/\lambda = 0.2521$. This value is roughly 24 times higher than that of the fast light topological mode in the zigzag interface with the same design parameters.

Next, we calculated transmittance spectra for straight and Z-shaped waveguides based on the bearded interface by the two-dimensional finite difference time domain method. To unidirectionally excite the confined modes, we utilized a point-like circular dipole source arranged at a chiral point of the waveguide. The simulation domain was terminated with perfectly matched layers. Power transmittances were recorded using two detectors located right after the source and near the waveguide end. In the two simulation setups, the source and two detectors were carefully arranged so that propagation lengths between the detectors were fixed at a single value of 51.5 periods, and the relative positions of the source, detectors, and waveguide ends became the same. To avoid signal distortion due to reflection particularly for the trivial mode in the Z-shaped waveguide, the first detector in straight waveguide was used for normalizing the transmittance spectra. The computed spectra are shown in Fig. 3(b). For the straight path, we observed a flat transmittance curve across the entire transmission band. For the Z-shaped channel, a flat curve was also observed for the frequency band of the topological mode located below the BZ

edge frequency. Even in the slow light region, the transmittance coincides with that of the straight channel, except around the BZ edge frequency. In contrast, the entire frequency band of the trivial mode shows significant loss in the Z-shaped channel, predominantly stemming from reflection at the corners. To quantitatively evaluate transmittance in the slow light regime, we plot transmittance for the Z-shaped interface as a function of n_g, as shown in Fig. 3(c). In the slow light regime of $n_g < 60$, the transmittance remains flat. This remarkable result demonstrates robust light transmission in the topological slow light mode with suppressed reflection at the corners. In contrast, we observed severe loss in the regime of $n_g > 60$. This behavior is probably because the kink mode is not topologically protected near the BZ edge due to coupling to the trivial mode.

To visualize the reflectionless transmission in the topological slow light mode, we calculated a snap-shot field distribution of light that was excited by a continuous-wave circular dipole source and propagated through the Z-shaped VPhC waveguide with a high n_g of ~30, as shown in Fig. 3(d). This value of n_g is realized at $a/\lambda = 0.2514$. The field distribution does not show any beating in field intensity, suggesting the absence of the formation of standing waves in the waveguide. This observation confirms the robust light transmission in the slow light regime. For further clarifying the power of topological protection on the waveguide, it will be important to quantitatively evaluate light transmittance under the presence of various types of structural imperfections using more intensive numerical simulations [5].

In summary, we discussed how to realize slow light waveguides in Si-slab-based VPhCs, and we found that a topological edge state at a bearded interface can behave as a slow light waveguide within topological bandgap. By comparing the bearded and zigzag interfaces, we identified the origins of the confined modes at the bearded interface. With numerical simulations of the topological mode at the bearded interface, we demonstrate large n_gs over 100 and robust light propagation via sharp corners even in slow light regime of $n_g \sim 60$. We envision that the topologically protected slow light waveguides, capable of enhancing light–matter interactions by increasing local density of states, could provide a versatile platform for exploring novel phenomena in topological photonics induced by nonlinear optical materials [43] and active emitters [44].

Funding. JSPS KAKENHI (JP15H05700, JP15H05868, JP17H06138); JST CREST (JPMJCR19T1); The Asahi Glass Foundation Research Grant Program.

Disclosures. The authors declare no conflicts of interest.

REFERENCES

1. L. Lu, J. D. Joannopoulos, and M. Soljačić, Nat. Photonics **8**, 821 (2014).
2. A. B. Khanikaev and G. Shvets, Nat. Photonics **11**, 763 (2017).
3. T. Ozawa, H. M. Price, A. Amo, N. Goldman, M. Hafezi, L. Lu, M. C. Rechtsman, D. Schuster, J. Simon, O. Zilberberg, and I. Carusotto, Rev. Mod. Phys. **91**, 015006 (2019).
4. Z. Wang, Y. Chong, J. D. Joannopoulos, and M. Soljačić, Nature **461**, 772 (2009).
5. M. Hafezi, E. A. Demler, M. D. Lukin, and J. M. Taylor, Nat. Phys. **7**, 907 (2011).
6. M. Hafezi, S. Mittal, J. Fan, A. Migdall, and J. M. Taylor, Nat. Photonics **7**, 1001 (2013).
7. A. B. Khanikaev, S. H. Mousavi, W. K. Tse, M. Kargarian, A. H. MacDonald, and G. Shvets, Nat. Mater. **12**, 233 (2013).
8. W. J. Chen, S. J. Jiang, X. D. Chen, B. Zhu, L. Zhou, J. W. Dong, and C. T. Chan, Nat. Commun. **5**, 5782 (2014).
9. L. H. Wu and X. Hu, Phys. Rev. Lett. **114**, 223901 (2015).
10. Y. Yang, Y. F. Xu, T. Xu, H.-X. Wang, J.-H. Jiang, X. Hu, and Z. H. Hang, Phys. Rev. Lett. **120**, 217401 (2018).
11. S. Yves, R. Fleury, T. Berthelot, M. Fink, F. Lemoult, and G. Lerosey, Nat. Commun. **8**, 16023 (2017).
12. S. Barik, A. Karasahin, C. Flower, T. Cai, H. Miyake, W. DeGottardi, M. Hafezi, and E. Waks, Science **359**, 666 (2018).
13. T. Ma and G. Shvets, New J. Phys. **18**, 025012 (2016).
14. X. D. Chen, F. L. Zhao, M. Chen, and J. W. Dong, Phys. Rev. B **96**, 020202 (2017).
15. X. D. Chen, W. M. Deng, J. C. Lu, and J. W. Dong, Phys. Rev. B **97**, 184201 (2018).
16. M. I. Shalaev, W. Walasik, A. Tsukernik, Y. Xu, and N. M. Litchinitser, Nat. Nanotechnol. **14**, 31 (2019).
17. X. T. He, E. T. Liang, J. J. Yuan, H. Y. Qiu, X. D. Chen, F. L. Zhao, and J. W. Dong, Nat. Commun. **10**, 872 (2019).
18. T. Yamaguchi, Y. Ota, R. Katsumi, K. Watanabe, S. Ishida, A. Osada, Y. Arakawa, and S. Iwamoto, Appl. Phys. Express **12**, 062005 (2019).
19. M. I. Shalaev, W. Walasik, and N. M. Litchinitser, Optica **6**, 839 (2019).
20. J. Ma, X. Xi, and X. Sun, Laser Photon. Rev. **13**, 1900087 (2019).
21. M. J. Mehrabad, A. P. Foster, R. Dost, A. M. Fox, M. S. Skolnick, and L. R. Wilson, arXiv:1912.09943 (2019).
22. Y. Gong, S. Wong, A. J. Bennett, D. L. Huffaker, and S. S. Oh, arXiv:2001.03661 (2020).
23. Y. Zeng, U. Chattopadhyay, B. Zhu, B. Qiang, J. Li, Y. Jin, L. Li, A. G. Davies, E. H. Linfield, B. Zhang, Y. Chong, and Q. J. Wang, Nature **578**, 246 (2020).
24. J. W. Dong, X. D. Chen, H. Zhu, Y. Wang, and X. Zhang, Nat. Mater. **16**, 298 (2017).
25. Z. Gao, Z. Yang, F. Gao, H. Xue, Y. Yang, J. Dong, and B. Zhang, Phys. Rev. B **96**, 201402 (2017).
26. F. Gao, H. Xue, Z. Yang, K. Lai, Y. Yu, X. Lin, Y. Chong, G. Shvets, and B. Zhang, Nat. Phys. **14**, 140 (2018).
27. X. Wu, Y. Meng, J. Tian, Y. Huang, H. Xiang, D. Han, and W. Wen, Nat. Commun. **8**, 1304 (2017).
28. J. Noh, S. Huang, K. P. Chen, and M. C. Rechtsman, Phys. Rev. Lett. **120**, 063902 (2018).
29. Y. Yang, H. Jiang, and Z. H. Hang, Sci. Rep. **8**, 1588 (2018).
30. X. D. Chen, F. L. Shi, H. Liu, J. C. Lu, W. M. Deng, J. Y. Dai, Q. Cheng, and J. W. Dong, Phys. Rev. Appl. **10**, 044002 (2018).
31. Y. Kang, X. Ni, X. Cheng, A. B. Khanikaev, and A. Z. Genack, Nat. Commun. **9**, 3029 (2018).
32. Y. Yang, Y. Poo, R. X. Wu, Y. Gu, and P. Chen, Appl. Phys. Lett. **102**, 231113 (2013).
33. J. Chen, W. Liang, and Z. Y. Li, Phys. Rev. B **99**, 014103 (2019).
34. S. A. H. Gangaraj and F. Monticone, Phys. Rev. Lett. **121**, 093901 (2018).
35. X. D. Chen, Z. L. Deng, W. J. Chen, J. R. Wang, and J. W. Dong, Phys. Rev. B **92**, 014210 (2015).
36. J. Guglielmon and M. C. Rechtsman, Phys. Rev. Lett. **122**, 153904 (2019).
37. Y. Plotnik, M. C. Rechtsman, D. Song, M. Heinrich, J. M. Zeuner, S. Nolte, Y. Lumer, N. Malkova, J. Xu, A. Szameit, Z. Chen, and M. Segev, Nat. Mater. **13**, 57 (2014).
38. E. Kuramochi, M. Notomi, S. Hughes, A. Shinya, T. Watanabe, and L. Ramunno, Phys. Rev. B **72**, 161318 (2005).
39. S. Assefa, S. J. McNab, and Y. A. Vlasov, Opt. Lett. **31**, 745 (2006).
40. A. Mock, L. Lu, and J. O'Brien, Phys. Rev. B **81**, 155115 (2010).
41. I. Söllner, S. Mahmoodian, S. L. Hansen, L. Midolo, A. Javadi, G. Kiršanske, T. Pregnolato, H. El-Ella, E. H. Lee, J. D. Song, S. Stobbe, and P. Lodahl, Nat. Nanotechnol. **10**, 775 (2015).
42. S. Mahmoodian, K. Prindal-Nielsen, I. Söllner, S. Stobbe, and P. Lodahl, Opt. Mater. Express **7**, 43 (2017).
43. D. Smirnova, D. Leykam, Y. Chong, and Y. Kivshar, arXiv:1912.01784 (2019).
44. Y. Ota, K. Takata, T. Ozawa, A. Amo, Z. Jia, B. Kante, M. Notomi, Y. Arakawa, and S. Iwamoto, Nanophotonics **9**, 547 (2020).